Fast and Slow Groundwater Reservoir Dynamics Revealed by Seismic Velocity Changes and Bayesian ICA in a Taiwan Mountain Ridge

Non-peer reviewed preprint submitted to EarthArXiv

Luc Illien[1], **Jens M. Turowski**[1], **Christoff Andermann**[2], **Jannik F. Kühn**[3], **Jui-ming Chang**[4], **and Niels Hovius**[1]

[1]GFZ Helmholtz Centre for Geosciences, Potsdam, 14473, Germany
[2]Géosciences Rennes, Université de Rennes, CNRS, UMR 6118, Rennes, 35042, France
[3]Center Rivages Pro Tech, SUEZ Eau France, Bidart 64210, France
[4]Department of Civil Enginering, National Yang Ming Chiao Tung University, Taiwan

Correspondence: Luc Illien (lillien@gfz.de)

Abstract. Mountain block recharge (MBR) is an important but difficult-to-observe component of mountain water budgets, especially in steep terrain where groundwater measurements are sparse. In such settings, relative seismic velocity changes (dv/v) derived from ambient-noise interferometry provide a potential proxy for hydrological storage variations, but interpretation is complicated because each frequency band may reflect a mixture of processes acting at different depths and spatial scales. Here, we investigate whether multi-frequency dv/v can be used to constrain groundwater storage dynamics at the mountain front. We analyse continuous seismic data from a ridge-scale array in Wanrong, Taiwan, together with precipitation, discharge, and borehole groundwater records, for the period March 2015 to June 2016. Daily dv/v time series are estimated in four frequency bands. All bands show pronounced seasonal and event-scale variations, including a strong velocity decrease during the typhoon season, but they differ markedly in amplitude and temporal evolution. Lower-frequency bands correlate more strongly with groundwater levels in the Hualien plain, whereas higher-frequency bands correlate more strongly with groundwater levels near the mountain front, indicating that the observed dv/v signals reflect a superposition of hydrological responses with different characteristic depths and spatial supports. To separate these mixed signals, we apply a Bayesian Independent Component Analysis approach in which the multi-band dv/v observations are represented as a linear mixture of latent reservoir responses. The inversion resolves two distinct characteristic timescales, with posterior median values of $\tau_1 = 69$ days and $\tau_2 = 160$ days. Higher-frequency bands are dominated by the fast component, while lower-frequency bands show a larger contribution from the slow component. Event-wise partitioning of precipitation further suggests that a larger fraction of summer rainfall is routed to the slow reservoir during the typhoon season. These results show that multi-frequency seismic velocity monitoring, combined with Bayesian source separation, can resolve fast and slow groundwater storage dynamics in complex mountainous terrain. The approach provides a new observational constraint on MBR-related processes where direct hydrogeological observations are limited.

1 Introduction

Mountain regions are critical sources river discharge, sustaining large downstream populations and water-dependent ecosystems (Viviroli et al., 2007; Immerzeel et al., 2010). As land use intensifies in steep terrain and climate variability increases, it becomes increasingly important to understand how water is stored and transferred through mountain systems (Viviroli et al., 2020; Immerzeel et al., 2020;). A substantial fraction of mountain water can be transmitted from mountain ranges into sedimentary basins as deep groundwater, a process commonly referred to as *mountain block recharge* (MBR) (Markovich et al., 2019). Because MBR can represent a large component of catchment water budgets and can

modulate the impacts of land-use change and cryospheric retreat, constraining its dynamics is essential for both hydrological prediction and water-resource management (van Tiel et al., 2024). Yet direct observation remains notoriously difficult: groundwater flow is largely hidden from view, and the steep topography of mountain belts makes drilling and maintaining borehole networks expensive and logistically challenging. Consequently, many assessments of MBR rely primarily on modeling or indirect tracers rather than continuous, spatially distributed measurements (Markovich et al., 2019; Fu et al., 2022).

Over the past decade, ambient-noise seismic interferometry has emerged as a promising approach for monitoring groundwater storage changes (Lecocq et al., 2017; Clements and Denolle, 2018; Mao et al., 2022). The method uses the continuous seismic wavefield generated by natural sources (e.g., rivers and ocean microseisms) recorded at seismic stations (Sens-Schönfelder and Brenguier, 2019). By cross-correlating seismic ambient noise records, one can retrieve cross correlation functions and estimate relative seismic velocity changes, dv/v (Sens-Schönfelder and Wegler, 2006). Variations in groundwater content and pore pressure modify elastic moduli and effective stress, producing measurable dv/v that can act as a proxy for hydrological processes (Denolle et al., 2025). Seismometers are also comparatively easy to deploy in remote terrain, offering a practical complement to sparse borehole observations (Lecocq et al., 2017; Clements and Denolle, 2018).

However, applying dv/v to MBR in mountainous settings remains challenging. Complex, steep topography, strong lateral lithological contrasts, and multiple hydrological pathways can complicate the interpretation of dv/v time series, making it difficult to attribute their variations to a simple linear correlation with groundwater level alone (Illien et al., 2021). Furthermore, steep topography likely induces reverberations and scattering of the wavefield, such that applying a conventional sensitivity kernel is not straightforward when the wavelength is comparable to the scale of the topographic relief. These complications make it difficult to interpret dv/v using direct inversion or single-reservoir conceptual models that can be more successful in relatively homogeneous sedimentary basins (Clements and Denolle, 2018; Mao et al., 2025).

To address this challenge, we introduce a statistical source-separation framework that models the observed dv/v signal as a superposition of underlying hydrological components. We apply a Bayesian formulation of Independent Component Analysis (ICA) to jointly analyze dv/v across multiple frequency bands. This approach identifies a small number of independent time series that, when linearly combined, explain the observed multi-frequency dv/v signals, while also providing uncertainty estimates for both the component time series and their relative contributions. By exploiting the different frequency dependence of hydrological processes, Bayesian ICA offers a systematic framework for separating overlapping reservoir dynamics and quantifying how precipitation is partitioned between fast and slow storage components in a mountainous environments.

We apply our proposed inversion technique to identify the dynamics of potential multiple reservoirs in a MBR setting. We leverage an existing seismic array deployed on a mountain ridge close to Wanrong, Taiwan, originally installed to investigate ridge site effects (Rault et al., 2020). The array straddles the outlets of two steep catchments immediately upstream of the Hualien sedimentary plain (Figure 1), providing a rare opportunity to probe recharge and storage dynamics at the mountain front. The proximity of independent hydrological and meteorological records (including borehole water levels, precipitation, and discharge) provides external constraints for interpretation.

This paper is organized as follows. Section 2 introduces the Wanrong dataset and its hydrological context. Section 3 describes the seismic interferometry workflow used to estimate dv/vṠection 4 presents observed dv/v variations across frequency bands. Section 5 applies Bayesian ICA to isolate independent components and interprets them in terms of reservoir behavior. Section 6 discusses the assumptions behind our approach and the hydrological implications of our results.

2 Data and Hydrological Context

2.1 Seismic array and general context

Taiwan is a particularly suitable setting for this study because previous work already indicates that hydrologic storage there is both strongly variable and temporally complex. At the island scale, geodetic and hydrological observations reveal pronounced seasonal and interannual water-storage variations, while differences in seasonal amplitudes and phase lags relative to precipitation suggest that these signals reflect different response times associated with transient storage, infiltration, soil saturation, and runoff (Hsu et al., 2020). Long-term hydrograph analyses further show that streamflow in Taiwanese catchments can be decomposed into fast, intermediate, and slow components, indicating that catchment response integrates multiple flow pathways and storage timescales Yeh and Chen (2022). In parallel, geochemical and isotopic evidence from the nearby Liwu catchment ($\sim$ 50km to the north) suggests that deep groundwater contributes measurably to long-term discharge even in steep terrain Calmels et al. (2011). Taken together, these studies imply that mountain catchments in Taiwan reflect the superposition of several hydrological components.

Recent work in Taiwan further demonstrates that seismic velocity variations are sensitive to hydrological processes. Feng et al. (2021) related seasonal crustal seismic velocity changes to hydrologic forcing at the scale of Taiwan, and Lien et al. (2025) used time-variable seismic velocity to ex-

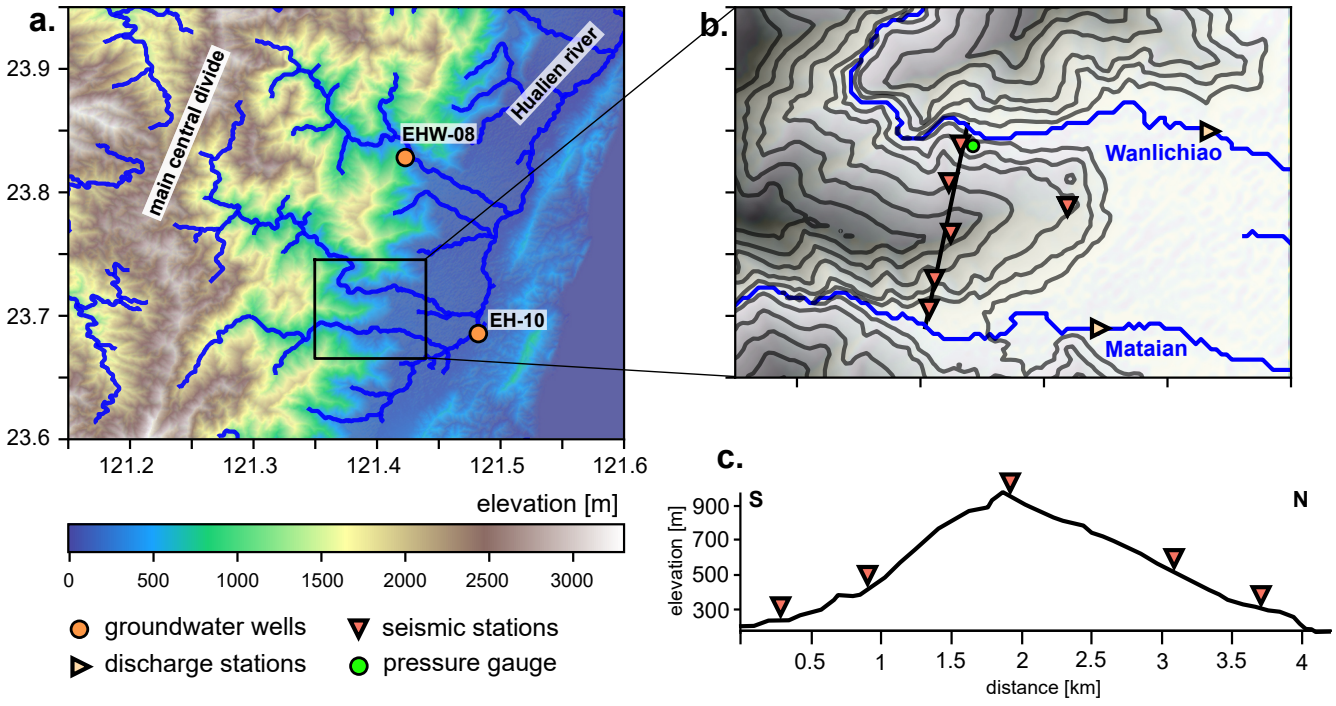

Figure 1. Study area and monitoring network in the Wanrong mountain-front region, Taiwan. (a) Regional topographic map showing the location of the study area between the main Central Range divide and the Hualien River, as well as the groundwater wells (EH-10 and EHW-08), discharge stations (Wanlichiao and Mataian), and the extent of the local study area shown in panel (b). (b) Map of the Wanrong ridge seismic array, including the seismic stations and the pressure gauge located in a small drainage. (c) South-to-north topographic profile of the ridge transect shown in panel (b), indicating the elevation of the seismic stations.

amine river–groundwater interactions in the southern Pingtung sedimentary plain. These studies establish the feasibility of using dv/v as a hydrologic proxy in Taiwan. Here, we extend that approach to a mountain ridge, where steep topography, fractured bedrock, and strong lithologic heterogeneity complicate interpretation but also make the setting particularly relevant for investigating how hydrologic storage is partitioned across multiple reservoirs at the mountain front.

Six broadband seismic stations (Trillium compact 120 s) were deployed along a mountain ridge near Wanrong Township in Hualien County (Figure 1), between the outlets of two steep catchments (the *Wanlichiao* and *Mataian* rivers; drainage areas of 242 and 136 km^2, respectively), immediately upstream of the Hualien sedimentary plain. The array was operated from March 2015 to June 2016, spanning a wet summer season and the subsequent winter, following a period of relative drought in Taiwan in 2014 (Hsu et al., 2020). The ridge has experienced past landsliding as the slopes are mantled by a mixture of weathering products, including soil and coarser debris. It is primarily underlain by schist (Central Geological Survey, Ministry of Economic Affairs (MOEA), 2008), with an estimated shear-wave velocity of about 3000 m s^{-1} (Lin et al., 1998; Kim et al., 2005). This setting provides an opportunity to investigate the transition from bedrock-dominated catchments to basin sediments, where MBR may contribute to regional groundwater storage.

2.2 Hydrometeorological and auxiliary datasets

We combine seismic observations with hydrometeorological datasets that provide independent constraints on storage and fluxes at multiple depths and spatial scales.

Groundwater level time series were obtained from Water Resources Agency, Ministry of Economic Affairs (2002). We use data from two regional boreholes that represent contrasting hydrogeologic settings: (i) borehole EH-10, located in the Hualien sedimentary plain approximately 9.5 km from the seismic array (Figure 1a), where the drilling log indicates predominantly sedimentary lithology; and (ii) borehole EHW-08, located near the adjacent mountain front approximately 15 km from the seismic array (Figure 1a), where the borehole was drilled mainly in metamorphic bedrock (schist). Each borehole is equipped with two piezometric sensors: a shallow sensor at 25 m depth and a deep sensor at 100 m depth.

Discharge records were obtained from gauging stations on the two rivers draining the ridge, operated by the Taiwan Water Resources Agency. In addition, a pressure gauge installed in a small stream draining the ridge provides a more local

proxy for flow initiation and short-timescale hydrological response, complementing the main river gauges.

We use precipitation from the GPM IMERG V7 gridded satellite product (Huffman et al., 2014), masked using watershed shapefiles for the Mataian and Wanlichiao catchments and averaged daily. We also use ERA5 reanalysis soil moisture and temperature (daily means) as proxies for shallow wetting and drying dynamics (Muñoz Sabater, 2019).

3 Estimation of relative seismic velocity changes

3.1 Methods

We estimate relative seismic velocity changes dv/v using ambient-noise interferometry. Continuous seismic records are divided into hourly segments, preprocessed by demeaning, bandpass filtering, and amplitude normalization through spectral whitening, and then cross-correlated to retrieve empirical Green's functions. We analyze four frequency bands: 0.5–1, 1–2, 2–4, and 4–8 Hz. For a pair of signals $u_a(t)$ and $u_b(t)$, the noise correlation function is written as

$$C_{ab}(\tau) = \int u_a(t)\, u_b(t+\tau)\, dt,$$

where τ is the lag time. Hourly correlation functions are then stacked within each day to obtain a daily correlation function $C_d(\tau)$, which is compared with a reference correlation function $C_{\mathrm{ref}}(\tau)$ constructed by stacking over a longer period, here taken as the full survey duration. This workflow is standard in ambient-noise monitoring and is implemented here using the SeisMIC Python package (Makus and Sens-Schönfelder, 2024).

We compute all correlation configurations permitted by the seismic array: (i) single-station cross-component correlations (SC), which correlate different components at the same station; (ii) single-station autocorrelations (AC), which correlate each component with itself; and (iii) interstation correlations (IC), which correlate records between station pairs across the ridge. Single-station cross-component correlations have previously been shown to recover seasonal dv/v variations in Taiwan (Feng et al., 2021).

Relative velocity changes are estimated with the stretching method (Sens-Schönfelder and Wegler, 2006) applied to the coda of the daily correlation functions. The method consists in finding the stretching factor ϵ that maximizes the similarity between the daily correlation function and a stretched version of the reference correlation function:

$$\rho(\epsilon) = \frac{\int_{t_1}^{t_2} C_d(t)\, C_{\mathrm{ref}}(t(1+\epsilon))\, dt}{\sqrt{\int_{t_1}^{t_2} C_d^2(t)\, dt}\, \sqrt{\int_{t_1}^{t_2} C_{\mathrm{ref}}^2(t(1+\epsilon))\, dt}}.$$

Here, t_1 and t_2 define the coda window over which the measurement is performed. The optimal stretching factor

$$\epsilon^* = \arg\max_{\epsilon} \rho(\epsilon)$$

corresponds, to first order, to the relative travel-time perturbation $\delta t/t$. Under the assumption that the perturbation is effectively homogeneous over the sensitivity region sampled by the coda, the relative seismic velocity change is then given by

$$\frac{dv}{v} \approx -\epsilon^*.$$

The coda window $[t_1, t_2]$ is defined separately for each frequency band so that measurements are made sufficiently late in the correlation function to emphasize scattered coda waves and avoid early source artefacts (Hobiger et al., 2014). For each band, we set t_1 to four times the longest period in the band, corresponding approximately to four wavelengths, and we use a window length of twelve wavelengths.The coda window $[t_1, t_2]$ is chosen separately for each frequency band. We set the start time t_1 to four times the longest period of the band, corresponding approximately to four wavelengths, and use a window duration of twelve wavelengths. This yields coda windows of 8–32 s for 0.5–1 Hz, 4–16 s for 1–2 Hz, 2–8 s for 2–4 Hz, and 1–4 s for 4–8 Hz.

For each frequency band, dv/v is first estimated independently for every available correlation configuration. For a given reference, this yields a similarity matrix $R_r(t_i, \epsilon_j)$, where t_i is the day index and ϵ_j is the tested stretching factor. Rather than selecting a separate dv/v estimate from each configuration and averaging them afterward, we combine the measurements at the level of the similarity matrices (Illien et al., 2022, 2023). Specifically, we stack the matrices $S_r(t_i, \epsilon_j)$ over all available configurations at a given frequency band, and determine the final daily dv/v from the stretching factor that maximizes the stacked similarity:

$$\bar{S}(t_i, \epsilon_j) = \frac{1}{N} \sum_{r=1}^{N} S_r(t_i, \epsilon_j),$$

where N is the number of available correlation configurations. The final daily velocity change is then obtained as

$$\left(\frac{dv}{v}\right)(t_i) = -\epsilon^*(t_i), \qquad \epsilon^*(t_i) = \arg\max_{\epsilon_j} \bar{R}(t_i, \epsilon_j).$$

This procedure provides a ridge-scale dv/v estimate for each frequency band and captures the average response of the ridge across frequencies.

4 Results: Frequency-dependent dv/v and hydrological observations

Figure 3 shows daily dv/v time series for the four frequency bands (0.5–1, 1–2, 2–4, and 4–8 Hz) together with precipitation and the pressure gauge located on the ridge.

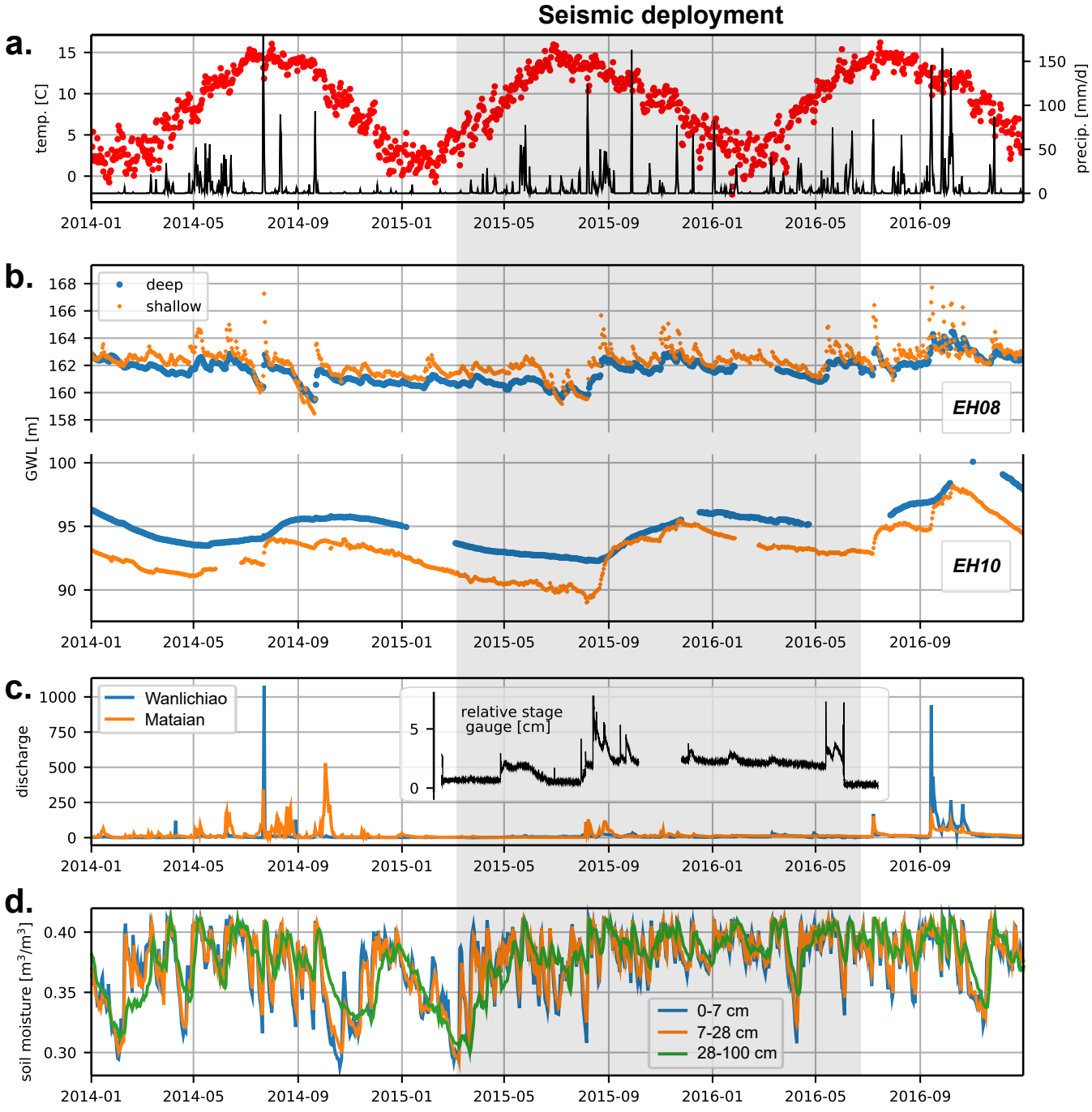

Figure 2. Hydrometeorological time series used to characterize the environmental forcing and hydrological response in the Wanrong ridge study area. (a) Air temperature and precipitation at the seismic deployment site between 2014 and 2016. (b) Groundwater levels in wells EHW-08 and EH-10, shown separately for shallow and deep piezometric sensors. (c) Discharge at the Wanlichiao and Mataian gauging stations, together with relative stage measured by the local pressure gauge in a small ridge drainage. (d) ERA5 soil moisture for the 0–7, 7–28, and 28–100 cm depth intervals. The grey shaded area marks the period analyzed in this study corresponding to the seismic deployment.

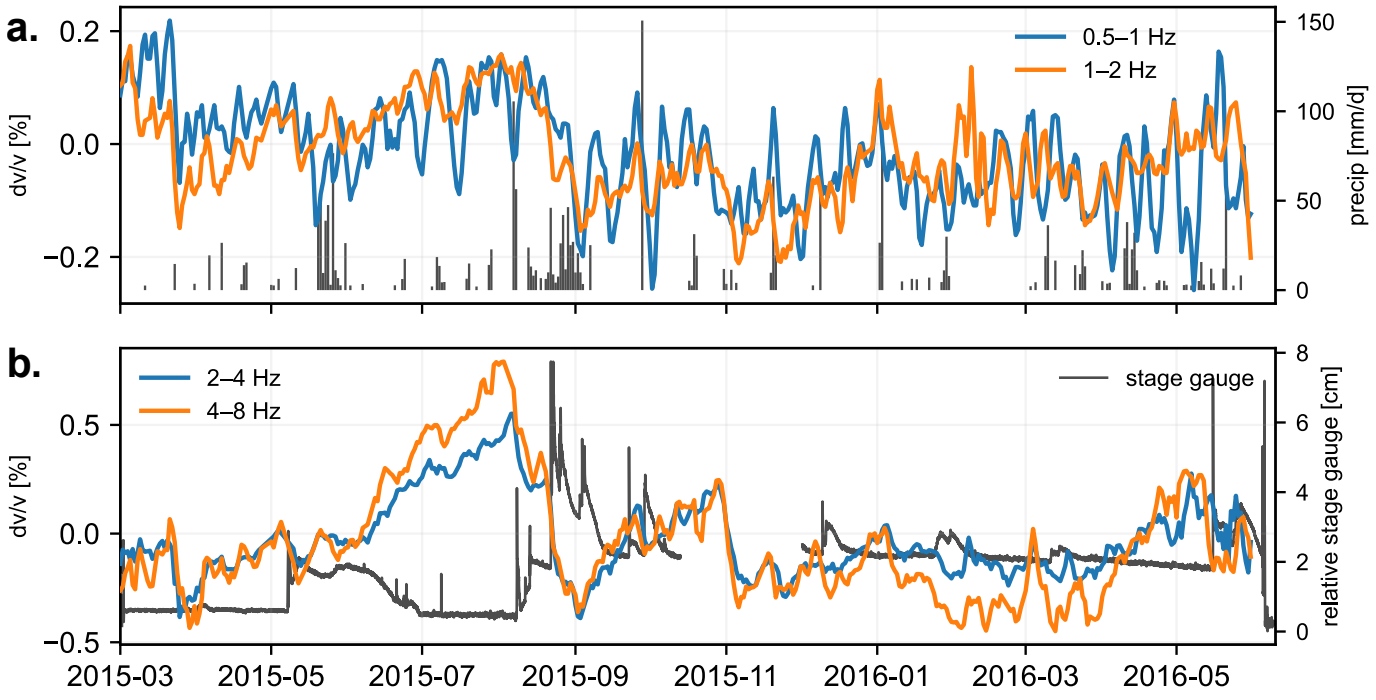

Figure 3. Time series of relative seismic velocity changes (dv/v) for the four frequency bands analyzed in this study. (a) Low-frequency bands (0.5–1 and 1–2 Hz) plotted together with daily precipitation. (b) High-frequency bands (2–4 and 4–8 Hz) plotted together with relative stage measured by the local pressure gauge. The dv/v variations show clear seasonal and event-scale fluctuations, with substantially larger amplitudes in the higher-frequency bands than in the lower-frequency bands.

A first-order observation is the strong contrast in dv/v amplitude across frequency bands. Low frequencies exhibit smaller variations: 0.5–1 and 1–2 Hz fluctuate by about 0.4% peak-to-peak. In contrast, higher-frequency bands show substantially larger excursions: 2–4 and 4–8 Hz reach peak-to-peak amplitudes of $\sim 1.3\%$ to 1.5%. Interpreting dv/v amplitudes in terms of depth sensitivity is not straightforward in steep topography; nevertheless, the larger high-frequency variations are consistent with enhanced sensitivity to shallow perturbations, where hydrological forcing is expected to be strongest in the shallow weathered subsurface.

All frequency bands show a pronounced velocity drop during the summer season, with the largest negative dv/v drop occurring in August 2015, coincident with intense precipitation (Figure 2a). This timing is consistent with concurrent rises in groundwater level in both boreholes and increased discharge at the river gauges (Figure 2bc). Beyond amplitude, the temporal structure of dv/v differs with frequency. While all bands share the major summer drop and subsequent recovery, the detailed shapes of the time series vary across bands. Notably, 2–4 and 4–8 Hz exhibit very similar temporal evolution, suggesting that they are influenced by a common set of processes and/or sample overlapping sensitivity volumes. In contrast, 0.5–1 and 1–2 Hz show more distinct dynamics, implying a different mixture of hydrological controls at lower frequencies.

To quantify the correspondence between seismic and hydrological storage proxies, we compute the Pearson correlation coefficient between dv/v and the groundwater-level time series for each borehole (Figure 4). As expected, dv/v is negatively correlated with groundwater level, because higher groundwater levels increase pore pressure, reduce effective stress, and thereby lower shear-wave velocity in the ridge (Fokker et al., 2021). Correlation strength depends on both frequency band and borehole location, and each frequency shows a distinct pattern of correlation with the two boreholes. At low frequency, 0.5–1 Hz shows the strongest correlation with EH-10, the borehole located in the Hualien sedimentary plain, which integrates flow over a larger upstream area and is therefore more representative of basin-scale groundwater fluctuations. In contrast, at higher frequency, 2–4 Hz shows a clearly stronger correlation with EHW-08, the borehole located in the adjacent valley and drilled in schist, consistent with a more local and shallower storage control. More broadly, the higher-frequency bands (2–4 and 4–8 Hz) tend to correlate more strongly with the mountain-front borehole, whereas the lower-frequency bands correlate better with the borehole in the Hualien plain. These frequency-dependent correlations support the interpretation that the multi-band dv/v observations reflect a mixture of reservoir dynamics sampled at different characteristic depths.

The relation between storage proxies (dv/v and groundwater levels) and river discharge is not straightforward. While

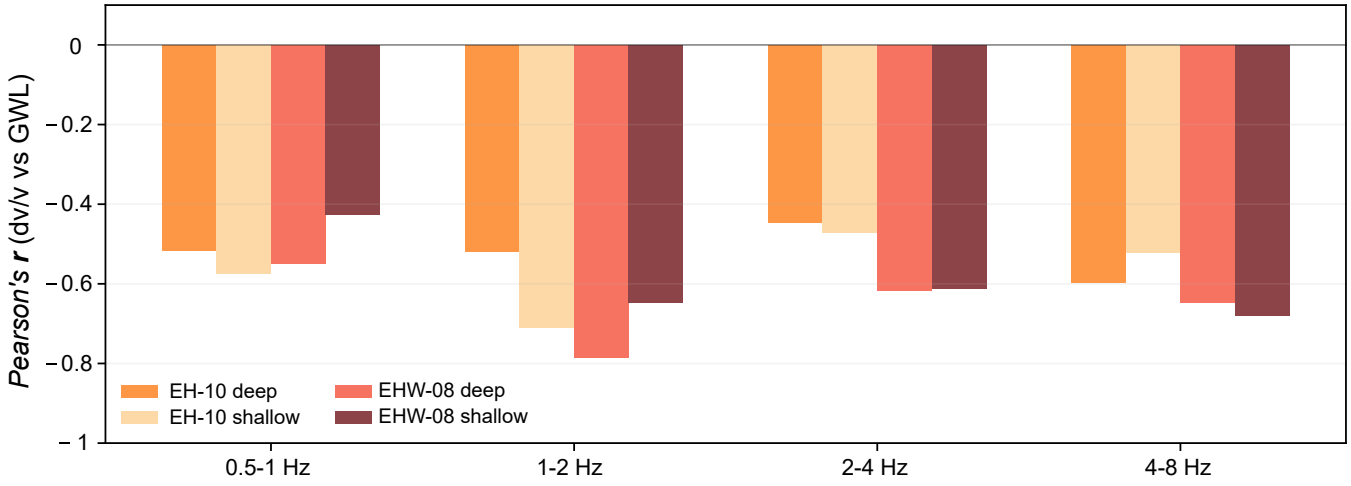

Figure 4. Pearson correlation coefficients between relative seismic velocity changes (dv/v) and groundwater levels for the four analyzed frequency bands. Results are shown separately for shallow and deep screened intervals in wells EH-10 and EHW-08. The systematic variation in correlation strength across frequency bands supports the interpretation that the multi-band dv/v observations integrate hydrological responses with different characteristic depths and spatial supports.

major precipitation events often coincide with discharge peaks, not all inferred recharge episodes (e.g., groundwater rises or dv/v drops) produce proportional increases in runoff at the river gauges. Notably, the pressure gauge on the ridge recorded an activation of the stream when the seismic velocity dropped and remained high for the rest of the period after september 2015. This indicates that the site may have been particularly dry before the recharge in August 2015 following the drought of 2014 (Hsu et al., 2020). This drought is also reflected in the soil moisture time-serie (Figure 2d), which showed a dip between September 2014 to September 2015.

Taken together, the results indicate that dv/v is strongly frequency dependent in both amplitude and temporal evolution, and that different bands preferentially track different groundwater observations. This supports the central hypothesis that each dv/v band records a superposition of hydrological dynamics integrated over different depths within the ridge. In the following section, we use Bayesian ICA to disentangle these mixed signals into two independent components interpretable as fast and slow reservoir responses.

5 Bayesian ICA on seismic velocity changes to disentangle hydrological reservoirs

5.1 Why Bayesian ICA on seismic velocity changes?

Ambient-noise based measurements of relative seismic velocity changes, dv/v, are commonly estimated in several frequency bands. Each band is sensitive to a range of depths and physical processes, and therefore integrates the potential effect of hydrological changes, thermal stress or earthquake damage to cite a few. In the context of hydrology and assuming the presence of multiple groundwater storage, we assume that the observed band-limited time series rarely correspond to a single physical reservoir; instead, they reflect an unknown mixture of underlying dynamical components as illustrated on Figure 5.

A classical approach to disentanglement would rely on sensitivity kernels (e.g., depth- or process-dependent kernels, Mao et al. (2025)) and a forward model linking environmental forcing to elastic property changes (Fokker et al., 2021). In many deployments, however, the necessary kernel information is either uncertain, incomplete, or strongly site-dependent (e.g., due to heterogeneous near-surface structure). Here, rather than prescribing sensitivity kernels, we adopt a *blind* but physically informed decomposition, where each frequency band is modeled as a mixture of a small number of independent latent reservoir responses, an approach that is widely used in geodesy through Independent Component Analysis methods (Gualandi et al., 2016; Xiong et al., 2024). The mixture is controlled by band-specific mixing coefficients, denoted c_f, which play the role of effective sensitivities and are learned jointly with the corresponding reservoir dynamics in a Bayesian framework (Roberts and Choudrey, 2005). Using a Bayesian framework to decompose dv/v time-series was also used in Parkfield, California (Okubo et al., 2024) but it is the first time to our knowledge that it is used to disentangle multiple hydrological reservoir with dv/v measured at multiple frequencies. A general formulation of the problem can given in the following.

Let $dv/v_f(t)$ be the observed dv/v time series in frequency band $f \in \{1, \ldots, F\}$ (with $F = 4$ in this work). We model each band as a linear superposition of latent reservoir re-

sponses $R_k(t)$ weighted by the mixing coefficients $w_{f,k}$:

$$\widehat{dv/v}_f(t) \;=\; \sum_{k=1}^{K} w_{f,k}\, R_k(t), \qquad w_{f,k} \geq 0, \quad \sum_{k=1}^{K} w_{f,k} = 1, \tag{1}$$

where K is the number of latent reservoirs. In the special two-reservoir case ($K = 2$), taken in our study, this reduces to

$$\widehat{dv/v}_f(t) \;=\; c_f\, R_1(t) + \big(1 - c_f\big)\, R_2(t), \qquad c_f \in (0,1). \tag{2}$$

The coefficients c_f are inferred from the data and summarize how strongly each frequency band loads on the "fast" versus "slow" reservoir response. The decomposition is then used as a generative model within a Bayesian inference framework. The Bayesian framework is useful here because it enables uncertainty quantification and makes it possible to evaluate whether the decomposition is actually well constrained by the data. In this sense, the mixing coefficients also implicitly account for the net physical changes integrated over the unknown sensitivity kernels sampled by each frequency band 5.

5.2 Bayesian formulation: posterior, likelihood, and noise model

Let $D = \{dv/v_f(t)\}$ denote the multi-band dv/v observations for frequency bands $f = 1, \ldots, F$ and times $t = 1, \ldots, T$. We seek the posterior distribution of the model parameters and latent variables, denoted collectively by θ, given the observations:

$$p(\theta \mid D) \;=\; \frac{p(D \mid \theta)\, p(\theta)}{p(D)} \;\propto\; p(D \mid \theta)\, p(\theta), \tag{3}$$

where $p(D \mid \theta)$ is the likelihood, that is, the probability of the observed dv/v data given a particular choice of parameters and latent reservoir responses; $p(\theta)$ is the prior, which encodes our assumptions about plausible parameter values before considering the data; and $p(D)$ is the evidence, a normalizing constant that ensures the posterior integrates to one (and is not required explicitly for the Markov Chain Monte Carlo (MCMC) sampling described in Appendix B). The posterior distribution $p(\theta \mid D)$ therefore represents the updated probability of the parameters and latent reservoir responses after combining prior assumptions with the information contained in the observations. We sample this posterior distribution using an MCMC algorithm, which is described in Appendix B, with the prior distributions adopted for all parameters given in Appendix A.

5.2.1 Reservoir dynamics driven by precipitation.

Each latent response is generated by convolving precipitation inputs with an exponential recession kernel (Sens-Schönfelder and Wegler, 2006; Hillers et al., 2014) with time scale τ_k,

$$R_k(t;\theta) \;=\; \sum_{t' \leq t} I_k(t') \exp\!\left(-\frac{t - t'}{\tau_k}\right) \;+\; R_{k0} \exp\!\left(-\frac{t}{\tau_k}\right), \tag{4}$$

This formulation makes it possible to infer how precipitation is partitioned between reservoirs with different characteristic recession times, and therefore to assess toward which storage components the incoming water is preferentially routed. Here, $I_k(t') \geq 0$ are precipitation amplitudes assigned to reservoir k at event times and $R_{k0} \geq 0$ is an optional initial-condition term. Event amplitudes are partitioned conservatively from a prior precipitation series $r(t)$:

$$I_1(t_i) = p_i\, r(t_i), \qquad I_2(t_i) = (1 - p_i)\, r(t_i), \tag{5}$$

with $p_i \in (0,1)$ inferred for each event t_i (details in Appendix A).

5.2.2 Likelihood and Gaussian noise assumption.

Because absolute dv/v amplitudes can differ across frequency bands due to processing choices and unknown gains, our primary inversions use a *shape-only* likelihood. We transform both observations and predictions to a common normalized space:

$$\begin{aligned} dv/v_f^{\star}(t) &= \mathrm{Norm}\big(dv/v_f(t)\big), \\ \widehat{dv/v}_f^{\,\star}(t;\theta) &= \mathrm{Norm}\Big(\widehat{dv/v}_f(t;\theta)\Big), \end{aligned} \tag{6}$$

where $\mathrm{Norm}(\cdot)$ denotes de-meaning and normalization by the root mean square of the data. We then assume independent Gaussian residuals for each frequency band:

$$dv/v_f^{\star}(t) \;=\; \widehat{dv/v}_f^{\,\star}(t;\theta) + \varepsilon_f(t), \qquad \varepsilon_f(t) \sim \mathcal{N}(0, \sigma_f^2), \tag{7}$$

with band-dependent noise scales σ_f. Under this assumption, the likelihood is the product of Gaussian probabilities over all times and frequency bands; for convenience, we work with its logarithm, which converts this product into a sum. The log-likelihood is

$$\begin{aligned} \log p(D \mid \theta) = \sum_{f=1}^{F} \sum_{t=1}^{T} \Big[&-\frac{1}{2} \log\big(2\pi\sigma_f^2\big) \\ &- \frac{1}{2\sigma_f^2} \Big(dv/v_f^{\star}(t) - \widehat{dv/v}_f^{\,\star}(t;\theta) \Big)^2 \Big]. \end{aligned} \tag{8}$$

We apply the Bayesian ICA framework to the multi-band dv/v observations using $K = 2$ latent reservoirs. Posterior inference is performed with five independent MCMC chains; after discarding burn-in and pooling samples, we obtain stable and well-converged posterior distributions for the key parameters (Figures 6).

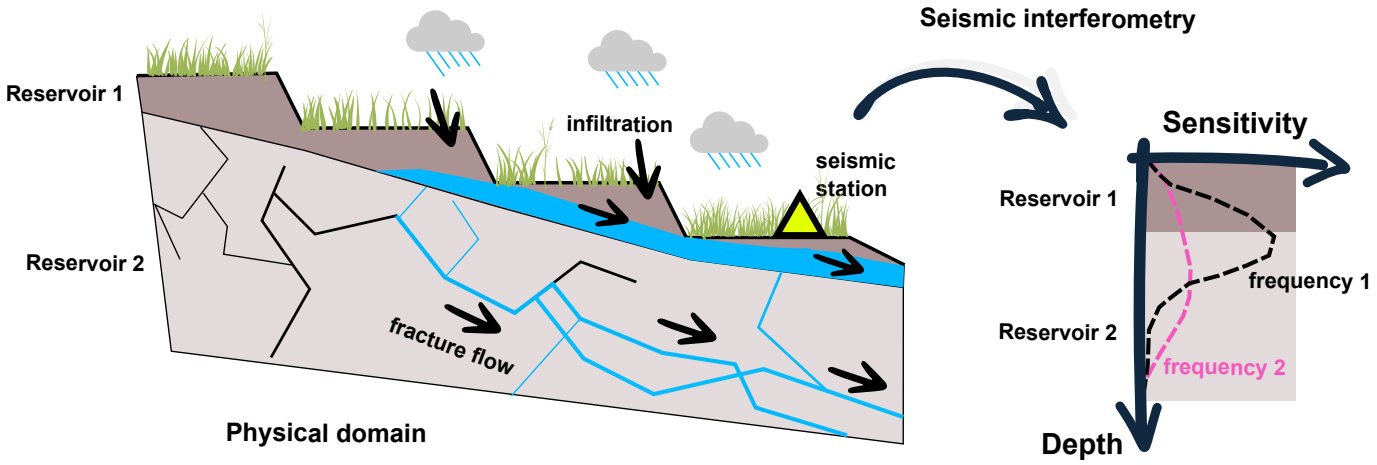

Figure 5. Conceptual framework linking hydrological storage and seismic observations. In the conceptual hillslope model, precipitation infiltrates into the subsurface and is partitioned between a shallow and a deeper reservoir, with flow partly transmitted through fractures. Seismic interferometry records the resulting relative seismic velocity changes, while different frequency bands sample different depth sensitivities and therefore different mixtures of the two reservoir responses.

5.3 Results: Bayesian ICA separation of fast and slow reservoirs

5.3.1 Reservoir timescales

The two-reservoir model yields two well-defined and non-overlapping posterior distributions for the characteristic recession timescales. The fast reservoir exhibits a posterior median of $\tau_1 = 69$ days, while the slow reservoir exhibits a posterior median of $\tau_2 = 160$ days (Figure 6a). The clear separation between τ_1 and τ_2 indicates that the data support two distinct reservoir timescales rather than a single broad characteristic timescale. The corresponding latent reservoir responses $R_1(t)$ and $R_2(t)$ are shown in Figure 7a; $R_1(t)$ responds rapidly to forcing and decays over weeks, whereas $R_2(t)$ integrates forcing over longer periods and decays over several months.

5.3.2 Fit to frequency-dependent dv/v time series

For each frequency band f, the model predicts $\widehat{dv/v}_f(t) = c_f R_1(t) + (1 - c_f) R_2(t)$ (Eq. 2). Overall, the two-reservoir mixture reproduces the observed seasonal evolution and event-scale modulations in dv/v across bands (Figure 7). Agreement is particularly strong during the main recharge and recession phases spanning the rainy season in August-September 2015 and subsequent recovery. Deviations are most apparent from November to February, where the model underfits portions of the observed variability. These misfits likely reflect processes not represented in the present two-reservoir formulation, such as the assumption that precipitation input enters the reservoirs without additional losses, and motivate the discussion in Section 6.

5.3.3 Frequency-dependent mixing coefficients

The band-specific mixing coefficient c_f, interpretable as the relative sensitivity of frequency band f to the fast reservoir compared to the slow reservoir, shows a systematic frequency dependence (Figure 6b). For the highest-frequency bands, 2–4 and 4–8 Hz, the posterior distributions of c_f are concentrated near 1, indicating that these bands are dominated by the fast reservoir signal. At lower frequencies, the posterior medians shift toward smaller values: $c_f \approx 0.74$ for 1–2 Hz and $c_f \approx 0.66$ for 0.5–1 Hz. This trend indicates an increasing contribution of the slow reservoir at lower frequencies, consistent with the expectation that lower-frequency dv/v integrates a larger fraction of deeper and/or more spatially extensive storage dynamics.

5.3.4 Shape-noise levels across bands

Posterior estimates of the band-dependent shape-noise scale σ_f also vary systematically with frequency (Figure 6c). Higher-frequency bands exhibit smaller σ_f, i.e., higher signal-to-noise in the normalized likelihood, whereas lower-frequency bands exhibit larger σ_f. If the largest relative changes in elastic properties (and hence dv/v) occur predominantly at shallow depths, then one expects stronger hydrologic signal and improved effective SNR in the higher-frequency bands. This also implies that the true noise level at each frequency bands could be constant.

5.3.5 Precipitation partitioning between fast and slow storage

A key output of the inversion is the event-wise partition fraction p_i, which quantifies the fraction of forcing routed into the fast reservoir at each precipitation event (Eq. 5). In Fig-

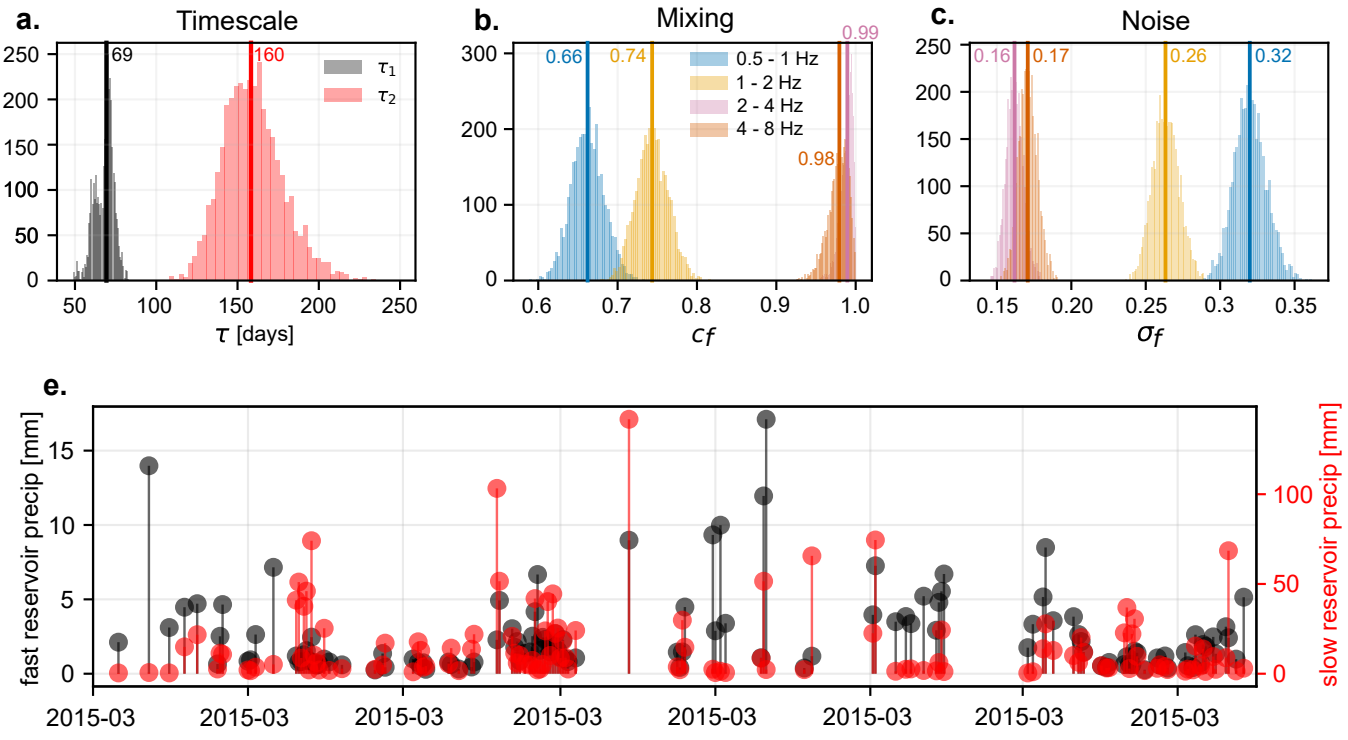

Figure 6. Results of the Bayesian ICA inversion. (a) Posterior distributions of the characteristic timescales of the fast and slow reservoirs, τ_1 and τ_2. (b) Posterior distributions of the frequency-dependent mixing coefficients c_f, which quantify the relative sensitivity of each dv/v band to the fast reservoir. (c) Posterior distributions of the band-specific noise parameters σ_f. (e) Event-wise precipitation amounts partitioned between the fast and slow reservoirs by the inversion. The results show a clear separation of two reservoir timescales and systematic frequency dependence in both mixing and noise.

ure 6d, we plot this fraction multiplied by the precipitation prior, so that the displayed quantities correspond to the precipitation input assigned to each reservoir. Because the inversion is carried out in a normalized dv/v amplitude space, these time series are best interpreted through their temporal evolution and relative changes, rather than through their absolute amplitudes. The inferred partitioning exhibits seasonal structure: during summer, the median contribution routed to the fast reservoir is reduced relative to other periods, suggesting that a larger portion of precipitation is directed into the slower compartment during the rainy season. We return to potential interpretations in Section 6, including the role of antecedent wetness, transient connectivity, and shallow buffering that may modulate how rainfall is transmitted into fast versus slow pathways.

5.3.6 Comparison to a single-reservoir model

A model constrained to a single reservoir ($K = 1$) does not provide a satisfactory fit to the multi-band dv/v observations (Figure S1). In particular, a single timescale cannot simultaneously reproduce the rapid variations emphasized in the higher-frequency bands and the smoother, more persistent dynamics expressed at lower frequencies. This comparison supports the inference that at least two distinct storage timescales are required to explain the observed frequency dependence.

6 Discussion

6.1 Model assumptions, validity, and limitations

Our Bayesian ICA framework is intentionally simple: it aims to extract dominant storage timescales and their frequency-dependent mixing from multi-band dv/v without prescribing a detailed, site-specific sensitivity kernel. In the following, we discuss the assumptions made with our approach.

All precipitation enters the subsurface forcing.

In the current implementation, the total precipitation $r(t)$ amplitudes is partitioned into the fast and slow reservoirs (Eq. 5). In reality, a substantial fraction of rainfall is lost to evapotranspiration, and part of the input may generate overland flow directly to the river without contributing to storage. Incorporating ET explicitly would require either a calibrated water-balance model or additional data. We also do not con-

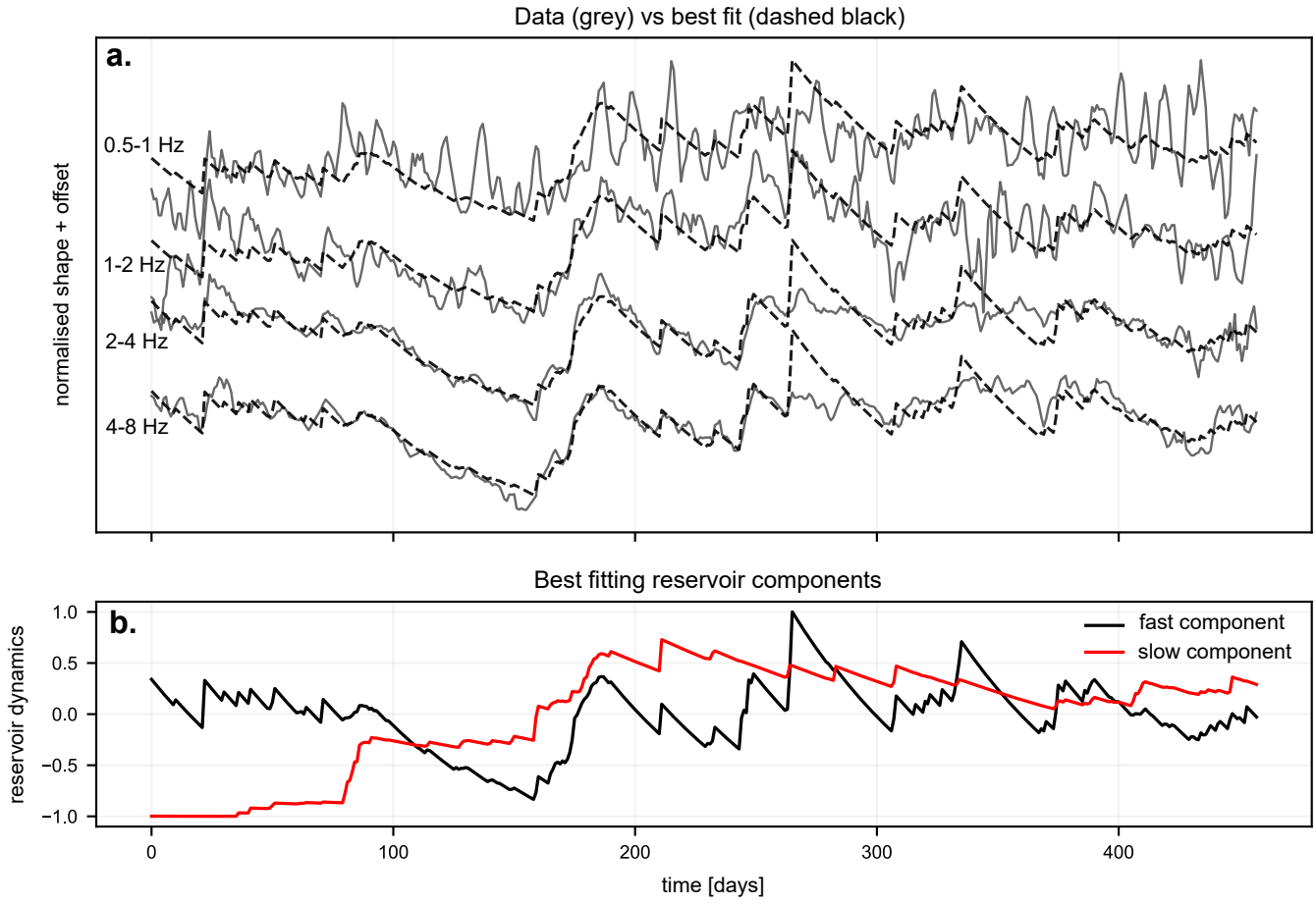

Figure 7. Best-fitting two-reservoir Bayesian ICA model for the multi-band dv/v observations. (a) Inferred latent reservoir dynamics, showing the fast and slow components obtained from the inversion. (b) Comparison between the observed dv/v time series (grey) and the best-fitting model predictions (dashed black) for the four analyzed frequency bands (0.5–1, 1–2, 2–4, and 4–8 Hz). The model reproduces the main seasonal and event-scale variations in the data, while highlighting the different relative contributions of the fast and slow reservoirs across frequency bands.

strain the link between rainfall amplitude and the amplitude of hydrologically induced dv/v. One could imagine a further flexible inversion in which event amplitudes were allowed to vary independently. While this can improve fit, it also increases the risk of overfitting by allowing the forcing to explain nearly all observed variability.

Independence of reservoirs and lack of exchange.

Our two-reservoir formulation assumes that the fast and slow compartments evolve independently and are only linked through precipitation partitioning. In reality, hillslope systems likely exhibit exchange (e.g., drainage from shallow storage feeding deeper groundwater and vice-versa) and state-dependent connectivity. Allowing exchange would introduce additional parameters (e.g., transfer coefficients) and could help explain periods of systematic misfit (e.g., November–February; Figure 7). However, we note that it makes our components truely independent, conceptually.

Linearity between storage and dv/v.

We assume that the contribution of each reservoir variable $R_k(t)$ to dv/v is linear (Eqs. 1–2). This assumption is intended as a first-order approximation, since seismic velocities may vary nonlinearly with water storage, pore pressure, and effective stress, and because the governing relationships may differ between the shallow regolith and the deeper fractured bedrock. Even so, the close agreement between modeled and observed band-limited dv/v over most of the record (Figure 7) indicates that the linear formulation captures the dominant temporal changes of the velocities.

Temperature and other non-hydrological influences.

We did not explicitly model temperature effects within the ICA inversion and instead rely on preprocessing and the expectation that hydrological forcing dominates annual dv/v variability at the studied frequencies. Residual thermoelastic contributions (Richter et al., 2014) and seasonal noise-source changes (Zhan et al., 2013) remain potential contributors, especially during winter months when rainfall forcing is weaker. Future work could explicitly include a temperature-driven component (e.g., an additional latent mode with a thermoelastic prior) and evaluate whether it reduces winter misfits without compromising identifiability of the hydrological reservoirs. We hypothesize that temperature may play an indirect role through not thermal stress but rather via the partitioning of precipitation p_i, which we captured in the inversion.

6.2 Methodological improvements and extensions

The framework is modular: while we used exponential recession to represent reservoir dynamics, other time-series models could be substituted (e.g., state-dependent drainage, or physically motivated unsaturated-zone transfer functions). A natural extension is to embed a more physical hydrological model with depth informations. Doing so robustly, however, requires additional constraints (e.g., distributed soil moisture, piezometric profiles, tracer-derived transit times, or site-specific sensitivity information for dv/v).

We also fixed the number of reservoirs to $K = 2$ to highlight both a fast and slow components. This number was justified by geochemistry studies in the Liwu catchment Calmels et al. (2011), where two reservoirs (a fast runoff and a deep groundwater) were constrained. An additional reservoir was coined as 'slow runoff' but is supposed to only be activated durnig typhoons, which did not occur during the deployment. A principled way to infer K would be to adopt a transdimensional Bayesian approach (e.g., reversible-jump MCMC such as used in tomographic inversion, Bodin et al. (2012)) or to compare models using predictive criteria (e.g., Watanabe–Akaike information criterion, WAIC) in a way that penalizes unnecessary complexity. Such approaches could objectively test whether an intermediate reservoir (or a dedicated thermoelastic component) is supported by the data.

6.3 Seasonal precipitation partitioning and hydrological interpretation

The inferred event-wise partitioning suggests that, during summer, a larger fraction of precipitation is routed into the slow reservoir than during other seasons (Figure 8). If the slow component reflects deeper and/or more spatially extensive storage (as implied by the lower-frequency mixing coefficients; Section 5.3.3), this points to enhanced deep recharge during the typhoon season.

A plausible mechanism is *state-dependent connectivity*: repeated rainfall during summer maintains high antecedent moisture and reduces soil-water deficits, increasing hydraulic connectivity and promoting deeper percolation and recharge. Above 200 mm of cumulative precipitation per month, most of the precipitation was routed to the slow reservoir, which suggest that the high precipitation may have brought the fast reservoir closer to saturation. In the Nepal Himalayas, subsurface moisture has been proposed as a key regulator of groundwater recharge and catchment-scale runoff generation under monsoon forcing (Illien et al., 2021), consistent with the idea that seasonal wetting can unlock deeper transfer pathways.

Within this conceptual picture, the fast reservoir likely reflects shallow, rapidly responding storage (e.g., near-surface regolith and perched zones) that drains over weeks, while the slow reservoir reflects deeper storage and longer recession over months. The summer shift toward slow routing may therefore reflect both more frequent and intense precipitation inputs and enhanced deep connectivity under persistently wet conditions.

6.4 Order-of-magnitude hydraulic diffusivities from recession timescales

Although aquifer geometry and boundary conditions are uncertain, the inferred recession timescales can be used to estimate an *effective* hydraulic diffusivity D (units $\mathrm{m^2\,s^{-1}}$) under a simple 1-D diffusion approximation (Carr and Simpson, 2018). For a characteristic length scale L, a common estimate of the dominant diffusion timescale is

$$\tau \approx \frac{L^2}{\pi^2 D}, \tag{9}$$

which yields

$$D \approx \frac{L^2}{\pi^2 \tau}. \tag{10}$$

Here, τ represents the characteristic relaxation time of hydraulic-head perturbations over the length scale L.

Taking $L = 1700$ m (ridge scale, Figure 1) gives:

- using $\tau_2 = 160$ days: $D \approx 2.1 \times 10^{-2}\ \mathrm{m^2\,s^{-1}}$,
- using $\tau_1 = 69$ days: $D \approx 4.7 \times 10^{-2}\ \mathrm{m^2\,s^{-1}}$.

These values are moderate-to-high and could be consistent with shallow saturated colluvium or highly transmissive near-surface deposits. This interpretation is plausible given that the ridge is affected by slope instabilities and landslide-related materials documented at the site.

If instead the relevant length scale is closer to the distance to the main divide (e.g., $L = 16$ km), then using $\tau_2 = 160$ days yields $D \approx 1.9\ \mathrm{m^2\,s^{-1}}$, an extremely high value

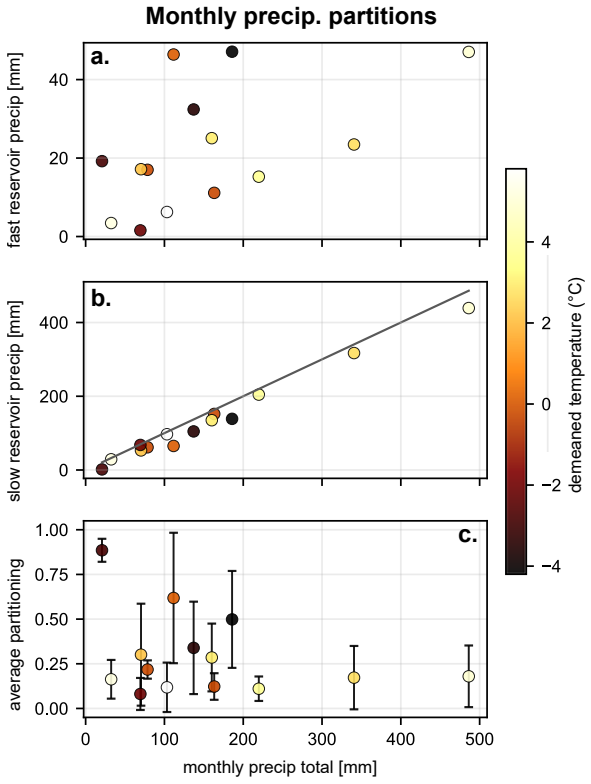

Figure 8. Relation between monthly precipitation partitioning and temperature. (a) Monthly precipitation amount assigned to the fast reservoir as a function of total monthly precipitation. (b) Monthly precipitation amount assigned to the slow reservoir as a function of total monthly precipitation; the grey line indicates the 1:1 relation. (c) Average monthly partitioning to the fast reservoir as a function of total monthly precipitation, shown with uncertainty bars. Marker colour indicates demeaned temperature. The figure suggests that warmer and wetter periods are associated with a larger proportion of precipitation routed to the slow reservoir.

more typical of pressure diffusion through fractured rock at larger scales (Andermann et al., 2012). This highlights a key uncertainty: τ is well constrained by the data, but L is not uniquely defined and may differ between the fast and slow components.

To help interpret the latent reservoirs, we plotted the inferred $R_k(t)$ time series against all available groundwater-level records (Figure 9). Reservoir component 1 is most consistent with boreholes located along the adjacent mountain front draining the neighboring catchment (EHW-08 on Figure 1), most of which are drilled in schist,with the top 10m being colluvium materials. Reservoir component 2, in contrast, shows greater correspondence with boreholes from the Hualien sedimentary plain EH-10 on Figure 1, suggesting an association with the shallower alluvial aquifer system. A notable exception occurs in June 2015, when rainfall caused a pronounced increase in reservoir component 2, whereas no comparable rise is observed in the borehole data. One possible explanation for this discrepancy is that evapotranspiration is not explicitly accounted for, leading the model to overestimate the fraction of rainfall contributing to temporary subsurface storage.

7 Conclusions

We used multi-frequency ambient-noise interferometry to track relative seismic velocity changes (dv/v) on a Taiwan mountain-front ridge and showed that the frequency dependence of dv/v reflects mixed hydrological dynamics rather than a single storage mode. A Bayesian ICA decomposition resolves two distinct reservoir timescales (posterior medians $\tau_1 = 69$ days and $\tau_2 = 160$ days) and reveals systematic, frequency-dependent mixing: higher frequencies primarily load on the fast reservoir, whereas lower frequencies show an increasing contribution from the slow reservoir. Event-wise partitioning further suggests seasonal modulation of recharge routing, with a larger fraction of summer precipitation routed into the slower compartment. Together, these results demonstrate that Bayesian ICA provides an interpretable, uncertainty-aware way to disentangle fast and slow groundwater storage dynamics from multi-band dv/v in complex mountainous terrain, offering a new observational constraint on MBR-related processes where direct monitoring is limited.

Code availability. The code for Bayesian inversion will be published on Github upon publication. We will also upload the parameter files used in the SeisMiC Python package for the estimation of dv/v

Data availability. Data will be made available upon publication.

References

Water Resources Research, Journal of the American Water Resources Association, 5, 2–2, https://doi.org/10.1111/j.1752-1688.1969.tb04897.x, 1969.

Andermann, C., Longuevergne, L., Bonnet, S., Crave, A., Davy, P., and Gloaguen, R.: Impact of transient groundwater storage on the discharge of Himalayan rivers, Nature Geoscience, https://doi.org/10.1038/NGEO1356ï, 2012.

Bodin, T., Sambridge, M., Rawlinson, N., and Arroucau, P.: Transdimensional tomography with unknown data noise, Geophysical Journal International, 189, 1536–1556, https://doi.org/10.1111/j.1365-246X.2012.05414.x, 2012.

Calmels, D., Galy, A., Hovius, N., Bickle, M., West, A. J., Chen, M.-C., and Chapman, H.: Contribution of deep groundwater to the weathering budget in a rapidly eroding mountain belt, Taiwan, Earth and Planetary Science Letters, 303, 48–58, https://doi.org/https://doi.org/10.1016/j.epsl.2010.12.032, 2011.

Carr, E. J. and Simpson, M. J.: Accurate and efficient calculation of response times for ground-

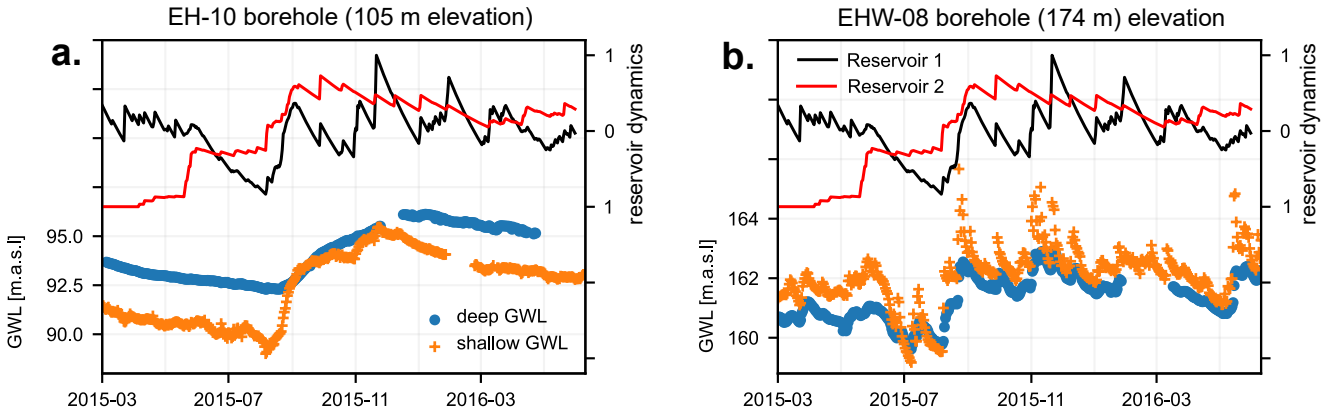

Figure 9. Comparison between inferred reservoir dynamics and groundwater-level variations in the two boreholes. (a) EH-10 borehole at 105 m elevation. (b) EHW-08 borehole at 174 m elevation. In each panel, the upper plot shows the inferred dynamics of Reservoir 1 and Reservoir 2, while the lower plot shows the groundwater level (GWL) time series for the deep and shallow screened intervals. The figure illustrates the temporal correspondence between the Bayesian ICA reservoir components and groundwater fluctuations at the two monitoring sites.

water flow, Journal of Hydrology, 558, 470–481, https://doi.org/https://doi.org/10.1016/j.jhydrol.2017.12.023, 2018.

Central Geological Survey, Ministry of Economic Affairs (MOEA): National Geological Data Warehouse, https://www.moeacgs.gov.tw/eng/Service/item_list?mid=169, 2008.

Clements, T. and Denolle, M. A.: Tracking Groundwater Levels Using the Ambient Seismic Field, Geophysical Research Letters, 45, 6459–6465, https://doi.org/10.1029/2018GL077706, 2018.

Denolle, M. A., Shi, Q., Clements, T., Viens, L., Rodriguez-Tribaldos, V., and Cotton, F.: Ambient field seismology in critical zone hydrological sciences, Comptes Rendus. Géoscience, 357, 425–451, https://doi.org/10.5802/crgeos.310, 2025.

Feng, K.-F., Huang, H.-H., Hsu, Y.-J., and Wu, Y.-M.: Controls on Seasonal Variations of Crustal Seismic Velocity in Taiwan Using Single-Station Cross-Component Analysis of Ambient Noise Interferometry, Journal of Geophysical Research: Solid Earth, 126, e2021JB022 650, https://doi.org/https://doi.org/10.1029/2021JB022650, e2021JB022650 2021JB022650, 2021.

Fokker, E., Ruigrok, E., Hawkins, R., and Trampert, J.: Physics-Based Relationship for Pore Pressure and Vertical Stress Monitoring Using Seismic Velocity Variations, Remote Sensing, 13, https://doi.org/10.3390/rs13142684, 2021.

Fu, Y., Dong, Y., Wang, L., Bour, O., Klepikova, M. V., Zong, Z., Xu, Z., and Zhou, Z.: Characteristics of hydraulic conductivity in mountain block systems and its effects on mountain block recharge: Insights from field investigation and numerical modeling, Journal of Hydrology, 612, 128 184, https://doi.org/https://doi.org/10.1016/j.jhydrol.2022.128184, 2022.

Gualandi, A., Serpelloni, E., and Belardinelli, M. E.: Blind source separation problem in GPS time series, Journal of Geodesy, 90, 323–341, https://doi.org/10.1007/s00190-015-0875-4, 2016.

Hillers, G., Campillo, M., and Ma, K.-F.: Seismic velocity variations at TCDP are controlled by MJO driven precipitation pattern and high fluid discharge properties, Earth and Planetary Science Letters, 391, 121–127, https://doi.org/https://doi.org/10.1016/j.epsl.2014.01.040, 2014.

Hobiger, M., Wegler, U., Shiomi, K., and Nakahara, H.: Single-station cross-correlation analysis of ambient seismic noise: application to stations in the surroundings of the 2008 Iwate-Miyagi Nairiku earthquake, Geophysical Journal International, 198, 90–109, https://doi.org/10.1093/gji/ggu115, 2014.

Hsu, Y.-J., Fu, Y., Bürgmann, R., Hsu, S.-Y., Lin, C.-C., Tang, C.-H., and Wu, Y.-M.: Assessing seasonal and interannual water storage variations in Taiwan using geodetic and hydrological data, Earth and Planetary Science Letters, 550, 116 532, https://doi.org/https://doi.org/10.1016/j.epsl.2020.116532, 2020.

Huffman, G., Bolvin, D., Braithwaite, D., Hsu, K., Joyce, R., and Xie, P.: Integrated Multi-satellitE Retrievals for GPM (IMERG), Version 4.4, ftp://arthurhou.pps.eosdis.nasa.gov/gpmdata/, accessed 31 March 2015, 2014.

Illien, L., Andermann, C., Sens-Schönfelder, C., Cook, K. L., Baidya, K. P., Adhikari, L. B., and Hovius, N.: Subsurface Moisture Regulates Himalayan Groundwater Storage and Discharge, AGU Advances, 2, https://doi.org/10.1029/2021av000398, 2021.

Illien, L., Sens-Schönfelder, C., Andermann, C., Marc, O., Cook, K. L., Adhikari, L. B., and Hovius, N.: Seismic Velocity Recovery in the Subsurface: Transient Damage and Groundwater Drainage Following the 2015 Gorkha Earthquake, Nepal, Journal of Geophysical Research: Solid Earth, 127, 1–18, https://doi.org/10.1029/2021jb023402, 2022.

Illien, L., Sens-Schönfelder, C., and Ke, K.-Y.: Resolving minute temporal seismic velocity changes induced by earthquake damage: the more stations, the merrier?, Geophysical Journal International, 234, 124–135, https://doi.org/10.1093/gji/ggad038, 2023.

Immerzeel, W. W., Van Beek, L. P., and Bierkens, M. F.: Climate change will affect the asian water towers, Science, https://doi.org/10.1126/science.1183188, 2010.

Immerzeel, W. W., Lutz, A. F., Andrade, M., Bahl, A., Biemans, H., Bolch, T., Hyde, S., Brumby, S., Davies, B. J., Elmore,

A. C., Emmer, A., Feng, M., Fernández, A., Haritashya, U., Kargel, J. S., Koppes, M., Kraaijenbrink, P. D., Kulkarni, A. V., Mayewski, P. A., Nepal, S., Pacheco, P., Painter, T. H., Pellicciotti, F., Rajaram, H., Rupper, S., Sinisalo, A., Shrestha, A. B., Viviroli, D., Wada, Y., Xiao, C., Yao, T., and Baillie, J. E.: Importance and vulnerability of the world's water towers, Nature, 577, 364–369, https://doi.org/10.1038/s41586-019-1822-y, 2020.

Kim, K.-H., Chiu, J.-M., Pujol, J., Chen, K.-C., Huang, B.-S., Yeh, Y.-H., and Shen, P.: Three-dimensional V_P and V_S structural models associated with the active subduction and collision tectonics in the Taiwan region, Geophysical Journal International, 162, 204–220, https://doi.org/10.1111/j.1365-246X.2005.02657.x, 2005.

Lecocq, T., Longuevergne, L., Pedersen, H. A., Brenguier, F., and Stammler, K.: Monitoring ground water storage at mesoscale using seismic noise: 30 years of continuous observation and thermo-elastic and hydrological modeling, Scientific Reports, 7, https://doi.org/10.1038/s41598-017-14468-9, 2017.

Lien, T.-Y., Chang, E. T.-Y., Cheng, H.-S., and Yeh, T.-K.: Unveiling river-groundwater interactions through time-variable seismic velocity in northern Pingtung Plain, southern Taiwan, Journal of Hydrology: Regional Studies, 58, 102 267, https://doi.org/https://doi.org/10.1016/j.ejrh.2025.102267, 2025.

Lin, C., Yeh, Y. H., Yen, H. Y., Chen, K., Huang, B., Roecker, S., and Chiu, J. M.: Three-dimensional elastic wave velocity structure of the Hualien region of Taiwan: Evidence of active crustal exhumation, Tectonics, 17, 103 – 89, https://api.semanticscholar.org/CorpusID:129567874, 1998.

Makus, P. and Sens-Schönfelder, C.: SeisMIC - an Open Source Python Toolset to Compute Velocity Changes from Ambient Seismic Noise, Seismica, 3, https://doi.org/10.26443/seismica.v3i1.1099, 2024.

Mao, S., Lecointre, A., Campillo, M., and Hilst, R. D. V. D.: Space-time monitoring of groundwater fl uctuations with passive seismic interferometry, pp. 1–9, https://doi.org/10.1038/s41467-022-32194-3, 2022.

Mao, S., Ellsworth, W. L., Zheng, Y., and Beroza, G. C.: Depth-dependent seismic sensing of groundwater recovery from the atmospheric-river storms of 2023, Science, 387, 758–763, https://doi.org/10.1126/science.adr6139, 2025.

Markovich, K. H., Manning, A. H., Condon, L. E., and McIntosh, J.: Mountain-Block Recharge: A Review of Current Understanding, Water Resources Research, 55, 8278–8304, https://doi.org/https://doi.org/10.1029/2019WR025676, 2019.

Muñoz Sabater, J.: ERA5-Land hourly data from 1950 to present, https://doi.org/10.24381/cds.e2161bac, accessed [date], 2019.

Okubo, K., Delbridge, B. G., and Denolle, M. A.: Monitoring Velocity Change Over 20 Years at Parkfield, Journal of Geophysical Research: Solid Earth, 129, 1–38, https://doi.org/10.1029/2023JB028084, 2024.

Rault, C., Chao, W.-A., Gélis, C., Burtin, A., Chang, J. M., Marc, O., Lai, T. S., Wu, Y., Hovius, N., and Meunier, P.: Seismic Response of a Mountain Ridge Prone to Landsliding, Bulletin of the Seismological Society of America, 110, 3004–3020, https://api.semanticscholar.org/CorpusID:225540062, 2020.

Richter, T., Sens-Schönfelder, C., Kind, R., and Asch, G.: Comprehensive observation and modeling of earthquake and temperature-related seismic velocity changes in northern Chile with passive image interferometry, Journal of Geophysical Research: Solid Earth, 119, 4747–4765, https://doi.org/10.1002/2013JB010695, 2014.

Roberts, S. and Choudrey, R.: Bayesian Independent Component Analysis with Prior Constraints: An Application in Biosignal Analysis, in: Deterministic and Statistical Methods in Machine Learning, edited by Winkler, J., Niranjan, M., and Lawrence, N., pp. 159–179, Springer Berlin Heidelberg, Berlin, Heidelberg, ISBN 978-3-540-31728-9, 2005.

Sens-Schönfelder, C. and Brenguier, F.: Noise-based Monitoring, in: Seismic Ambient Noise, edited by Nakata, N., Gualtieri, L., and Fichtner, A., chap. Noise-base, pp. 267–301, Cambridge University Press, 2019.

Sens-Schönfelder, C. and Wegler, U.: Passive image interferometry and seasonal variations of seismic velocities at Merapi Volcano, Indonesia, Geophysical Research Letters, 33, https://doi.org/https://doi.org/10.1029/2006GL027797, 2006.

van Tiel, M., Aubry-Wake, C., Somers, L., Andermann, C., Avanzi, F., Baraer, M., Chiogna, G., Daigre, C., Das, S., Drenkhan, F., Farinotti, D., Fyffe, C. L., de Graaf, I., Hanus, S., Immerzeel, W., Koch, F., McKenzie, J. M., Müller, T., Popp, A. L., Saidaliyeva, Z., Schaefli, B., Schilling, O. S., Teagai, K., Thornton, J. M., and Yapiyev, V.: Cryosphere–groundwater connectivity is a missing link in the mountain water cycle, Nature Water, 2, 624–637, https://doi.org/10.1038/s44221-024-00277-8, 2024.

Viviroli, D., Dürr, H. H., Messerli, B., Meybeck, M., and Weingartner, R.: Mountains of the world, water towers for humanity: Typology, mapping, and global significance, Water Resources Research, 43, https://doi.org/10.1029/2006WR005653, 2007.

Viviroli, D., Kummu, M., Meybeck, M., Kallio, M., and Wada, Y.: Increasing dependence of lowland populations on mountain water resources, Nature Sustainability, 3, 917–928, https://doi.org/10.1038/s41893-020-0559-9, 2020.

Water Resources Agency, Ministry of Economic Affairs: Integration project on groundwater monitoring and land subsidence prevention, institutional report, 2002.

Xiong, Y., Feng, W., Zhou, X., Kusche, J., Shen, Y., Yang, M., Wang, C., and Zhong, M.: Separation of earthquake and hydrology signals from GRACE satellites data via independent component analysis: a case study in the Sumatra region, Geophysical Journal International, 239, 1597–1616, https://doi.org/10.1093/gji/ggae351, 2024.

Yeh, H.-F. and Chen, H.-Y.: Assessing the long-term hydrologic responses of river catchments in Taiwan using a multiple-component hydrograph approach, Journal of Hydrology, 610, 127 916, https://doi.org/https://doi.org/10.1016/j.jhydrol.2022.127916, 2022.

Zhan, Z., Tsai, V. C., and Clayton, R. W.: Spurious velocity changes caused by temporal variations in ambient noise frequency content, Geophysical Journal International, 194, 1574–1581, https://doi.org/10.1093/gji/ggt170, 2013.

Appendix A: Priors and parameterization

A1 Observation model

We consider F frequency bands (here $F = 4$) and a daily time grid $t = 1, \dots, T$. Let $dv/v_f(t)$ denote the observed dv/v time series for band f.

In the two-reservoir model ($K = 2$), each band is modeled as a mixture of two latent reservoir responses:

$$\widehat{dv/v}_f(t) \;=\; c_f\, R_1(t) + \big(1 - c_f\big)\, R_2(t), \qquad c_f \in (0,1).$$

Because absolute dv/v amplitudes can vary across bands due to processing and unknown gain factors, the primary inference is performed in *shape space*. Each band is demeaned and normalized by its root mean square:

$$dv/v_f^\star(t) = \frac{dv/v_f(t) - \overline{dv/v_f}}{\mathrm{RMS}\Big(dv/v_f(t) - \overline{dv/v_f}\Big)}.$$

Model predictions are treated consistently. Let

$$R_k^\star(t) = \frac{R_k(t) - \overline{R_k}}{\mathrm{RMS}\big(R_k(t) - \overline{R_k}\big)}.$$

Then the band prediction in shape space is

$$\widehat{dv/v}_f^{\,\star}(t) = \mathrm{Norm}\big(c_f\, R_1^\star(t) + (1 - c_f)\, R_2^\star(t)\big),$$

where $\mathrm{Norm}(\cdot)$ denotes the same demean-and-RMS normalization as above. Residuals are modeled as Gaussian:

$$dv/v_f^\star(t) = \widehat{dv/v}_f^{\,\star}(t) + \varepsilon_f(t), \qquad \varepsilon_f(t) \sim \mathcal{N}(0, \sigma_f^2),$$

with band-dependent "shape-noise" scales σ_f.

A2 Latent reservoir dynamics

Hydrological forcing is represented by a nonnegative event prior series $r(t) \geq 0$, typically sparse in time (e.g., daily precipitation impulses). Reservoir k responds as an exponential recession with time constant τ_k:

$$R_k(t) = \sum_{t' \leq t} I_k(t') \exp\left(-\frac{t - t'}{\tau_k}\right),$$

where $I_k(t') \geq 0$ is the effective event amplitude routed to reservoir k at event time t'.

A2.1 Initial condition / tail term.

An optional initial condition term represents storage at the start of the study, implemented as a decaying exponential tail:

$$R_{k,0}(t) = R_{k0} \exp\left(-\frac{t}{\tau_k}\right), \qquad R_{k0} \geq 0,$$

so that $R_k(t) \leftarrow R_k(t) + R_{k,0}(t)$ when initial conditions are inferred.

A2.2 Ordered time scales.

To avoid label switching and maintain interpretability, we enforce

$$\tau_{\min} \leq \tau_1 < \tau_2 \leq \tau_{\max}.$$

In the implementation, (τ_1, τ_2) are generated from unconstrained variables (e.g., $(x_1, x_2) \in \mathbb{R}^2$) through a smooth, monotone mapping that guarantees ordering and bounds.

A3 Conservative precipitation partition

To ensure mass conservation and avoid unphysical changes to forcing magnitude, event amplitudes are partitioned conservatively:

$$I_1(t_i) = p_i\, r(t_i), \qquad I_2(t_i) = (1 - p_i)\, r(t_i), \tag{A1}$$

for event times t_i where $r(t_i) > 0$. This enforces $I_1(t_i) + I_2(t_i) = r(t_i)$ exactly for every event.

The partition fraction p_i must lie between 0 and 1. Rather than sampling p_i directly, we introduce an unconstrained variable $q_i \in \mathbb{R}$ and transform it through a logistic function:

$$p_i = \frac{1}{1 + \exp(-q_i)}.$$

This guarantees that p_i always remains in the interval $(0, 1)$. We interpret p_i as the *fast fraction* for event i.

A4 Priors

A4.1 Mixing coefficients c_f.

We use a Beta prior for the mixing coefficient c_f, since c_f must remain between 0 and 1:

$$c_f \sim \mathrm{Beta}(\alpha_c, \alpha_c), \qquad \alpha_c \geq 1.$$

This symmetric prior is centered on 0.5, so it does not favor either reservoir a priori, while still discouraging extreme values close to 0 or 1 unless they are required by the data.

A4.2 Event partition variables q_i.

We place a Gaussian prior on the unconstrained partition variables:

$$q_i \sim \mathcal{N}(0, s_q^2).$$

Because p_i is obtained from q_i through a logistic transform, this prior controls how strongly the partitioning is pulled toward an even split between the two reservoirs. When s_q is small, most values of q_i remain close to zero, which implies $p_i \approx 0.5$. Larger values of s_q allow more extreme values of q_i, and therefore make near-exclusive routing to one reservoir or the other ($p_i \approx 0$ or $p_i \approx 1$) more plausible.

A4.3 Time scales τ_1, τ_2.

The reservoir time scales must satisfy both physical bounds and the ordering constraint $\tau_1 < \tau_2$, so they are not sampled directly. Instead, we sample unconstrained variables (x_1, x_2) and map them to admissible values of (τ_1, τ_2) using the parameterization described above. We assign weakly informative priors to (x_1, x_2) (for example, independent Gaussian priors), which in turn induce a broad prior over the allowed range of (τ_1, τ_2). This choice keeps the prior flexible while ensuring that the fast reservoir remains faster than the slow reservoir.

A4.4 Noise scales σ_f.

We parameterize σ_f via $\log \sigma_f$ and apply a half-normal prior on σ_f (equivalently a log-density on $\log \sigma_f$):

$$\sigma_f \sim \mathrm{HalfNormal}(\sigma_{\mathrm{prior}}), \qquad \sigma_f > 0.$$

A4.5 Initial-condition amplitudes R_{k0}.

When inferred, $R_{k0} \geq 0$ receives a half-normal prior with scale $R_{0,\mathrm{prior}}$:

$$R_{k0} \sim \mathrm{HalfNormal}(R_{0,\mathrm{prior}}).$$

Appendix B: MCMC inference algorithm

This appendix describes the Metropolis–Hastings sampling scheme used to approximate the posterior distribution of parameters and latent states. The sampler cycles through a set of proposal moves that target different parameter blocks, accepting or rejecting each move based on the Metropolis criterion.

B1 State vector

For the two-reservoir model, the state at iteration s comprises:

- event-routing variables $q = (q_i)_{i=1}^{N}$ (one per precipitation event);
- time scales (τ_1, τ_2) (ordered and bounded);
- mixing weights $c = (c_f)_{f=1}^{F}$ with $c_f \in (0, 1)$;
- noise scales $\sigma = (\sigma_f)_{f=1}^{F}$;
- initial conditions (R_{10}, R_{20});

Given a state, event amplitudes are computed deterministically via $p_i = \sigma(q_i)$ and Eq. (A1), then latents $R_1(t), R_2(t)$ and predictions $\widehat{dv/v}_f(t)$ are computed via the convolution and mixing relations above.

B2 One MCMC sweep: step-by-step

A *sweep* consists of applying the following proposals in sequence. Let $\log \pi(\theta)$ denote the log-posterior (log-likelihood plus log-priors) for current state θ.

B2.1 (1) Local event update for q_i (single-event move).

Select an event index i and propose

$$q_i' = q_i + \eta, \qquad \eta \sim \mathcal{N}(0, \sigma_{q,\mathrm{local}}^2),$$

keeping other q_j unchanged. The proposal changes p_i and therefore modifies (I_1, I_2) at that event while preserving $I_1 + I_2 = r$ exactly. Reservoir latents are updated efficiently using precomputed convolution columns (through *design matrices*): only the contributions from event i change. Accept with probability

$$\alpha = \min\left\{1, \exp\left[\log \pi(\theta') - \log \pi(\theta)\right]\right\}.$$

B2.2 (2) Block event update for q (multi-event move).

To improve mixing when precipitation events cluster in time, select a group of event indices W and propose a common shift

$$q_W' = q_W + \delta, \qquad \delta \sim \mathcal{N}(0, \sigma_{q,\mathrm{block}}^2),$$

again preserving conservative partitioning at each event. Reservoir latents are updated using matrix–vector products restricted to the selected event group.

B2.3 (3) Mixing-weight update for c_f (band-wise).

For each band f, propose a random walk in u_f:

$$u_f' = u_f + \xi, \qquad \xi \sim \mathcal{N}(0, \sigma_c^2), \qquad c_f' = \sigma(u_f').$$

The Jacobian term for the logistic map is included in the log-posterior when sampling in u_f. The proposed value is accepted with probability

$$\alpha = \min\left(1, \exp\left[\log \pi(\theta') - \log \pi(\theta)\right]\right),$$

where $\pi(\theta)$ denotes the posterior density. This is the standard Metropolis acceptance rule.

B2.4 (5) Noise-scale update for σ_f (band-wise).

Propose random walks in $\log \sigma_f$:

$$\log \sigma_f' = \log \sigma_f + \zeta, \qquad \zeta \sim \mathcal{N}(0, \sigma_{\log \sigma}^2).$$

Accept/reject using the change in likelihood and the half-normal prior on σ_f.

B2.5 Initial-condition update

For initial conditions, propose random walks in $\log R_{k0}$ and update the corresponding exponential tail contributions $R_{k,0}(t)$ for $k = 1, 2$. Accept/reject using the change in likelihood and the prior on R_{k0}.

B2.6 (7) Time-scale update for (τ_1, τ_2).

Propose random walks in the unconstrained variables:

$$x_1' = x_1 + \nu_1, \qquad x_2' = x_2 + \nu_2, \qquad \nu_1, \nu_2 \sim \mathcal{N}(0, \sigma_\tau^2),$$

then map $(x_1', x_2') \mapsto (\tau_1', \tau_2')$ ensuring $\tau_1' < \tau_2'$ and bounds. Recompute the convolution kernels and design matrices for the proposed time scales, then recompute R_1', R_2' (using current q and IC terms). Accept/reject with the Metropolis criterion.

B2.7 (9) Storage, best-state tracking, and pooling.

Every sweeps, store the current parameters in a trace (including q for two-reservoir posterior predictive reconstructions). Separately track the maximum a posteriori state by comparing current log-posterior values, used for "best fit" plots. Multiple chains are assessed for convergence (trace overlap, $\hat{R}$) and pooled after discarding burn-in and excluding non-converged chains.

B3 One-reservoir special case

For the $K = 1$ model, the mixing coefficients and partition variables are removed: $dv/v_f(t)$ is explained by a single latent $R(t)$ with one time scale τ (and optional IC and temperature terms). The MCMC sweep is simplified by omitting the q- and c-updates, while retaining updates for τ, σ_f, and optional temperature/IC parameters.

Competing interests. The authors do no have competing interests.

Supplementary figures

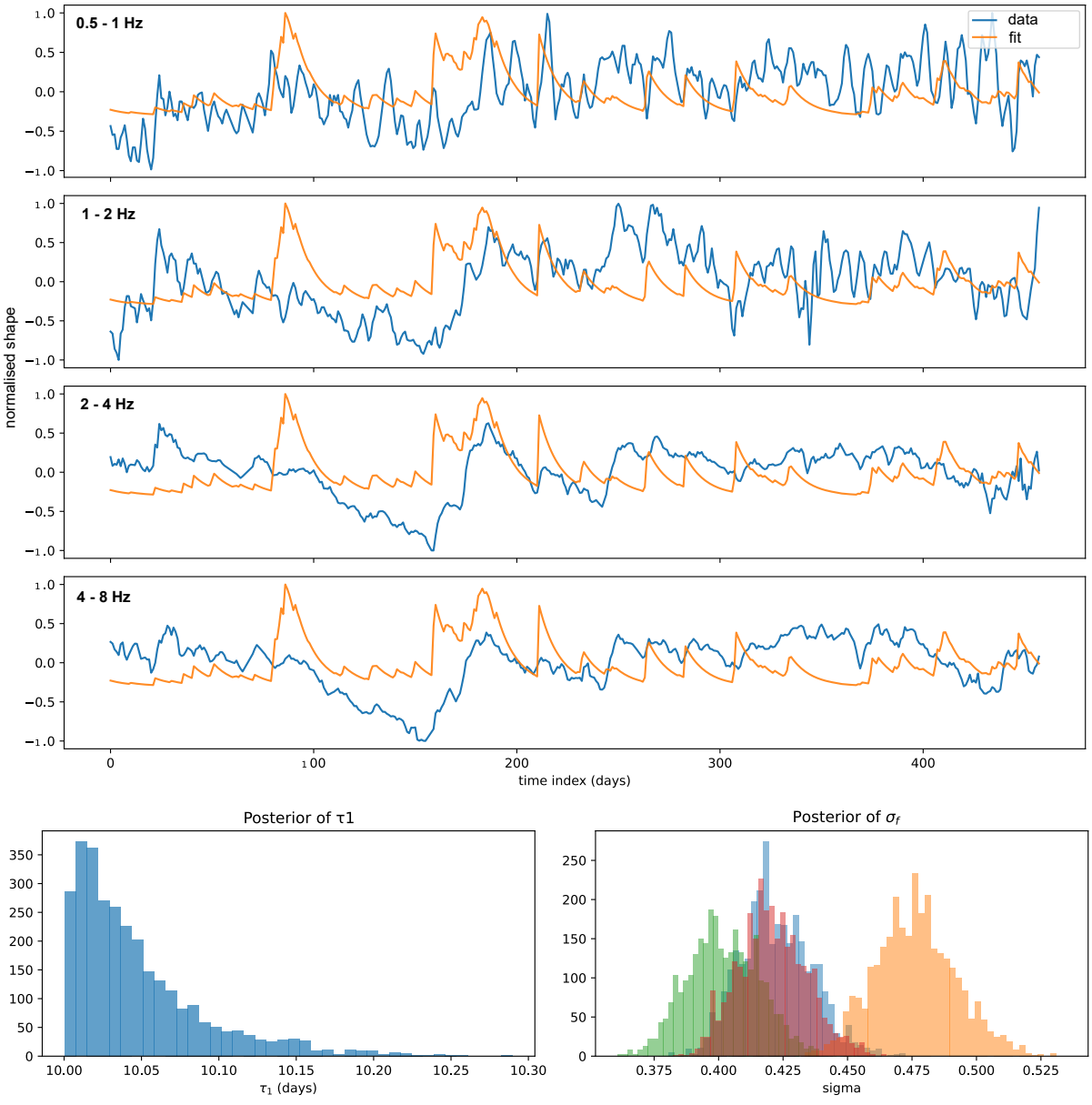

Figure S1. Fit of the single-reservoir ($K = 1$) Bayesian ICA model to the normalized multi-band dv/v observations. The upper panels compare the observed normalized dv/v time series (blue) with the best-fitting model predictions (orange) for the four analyzed frequency bands (0.5–1, 1–2, 2–4, and 4–8 Hz). The lower panels show the posterior distribution of the single reservoir timescale τ_1 and the posterior distributions of the band-specific noise parameters σ_f. The single-reservoir model does not reproduce the full frequency-dependent variability of the observations, supporting the need for at least two reservoirs to explain the multi-band dv/v dynamics.